

# X-RAY AND OPTICAL AFTERGLOWS IN GAMMA-RAY BURSTS: REFRESHED SHOCK AND JET EFFECTS

A. Panaiteescu, P. Mészáros

Department of Astronomy & Astrophysics, Pennsylvania State University, University Park, PA 16802

and

M. J. Rees

Institute of Astronomy, University of Cambridge, Madingley Road, Cambridge, CB3 0HA, U.K.

## ABSTRACT

We present an analytical approach to calculate the hydrodynamics of the interaction between a relativistic ejecta and a surrounding medium, whose evolution serves as a model for Gamma-Ray Burst afterglows. We investigate the effect of the relevant model parameters on the X-ray and optical fluxes, and the effect of a delayed energy input and anisotropy in the ejecta on the shape of the light curves. We compare our numerical results to observed afterglows and give a quantitative description of the conditions (geometry and physical parameters) in the ejecta that are compatible with the X-ray and optical light curves of the 970508 afterglow, for which a large number of accurate flux measurements are available.

*Subject headings:* gamma-rays: bursts - methods: numerical - radiation mechanisms: non-thermal

## 1. Introduction

Afterglows from Gamma-Ray Bursts (GRBs) have been observed from a number of objects at X-ray, optical, and in one case also at radio wavelengths. Simple analytical models are successful at explaining the major features of the light curves (Mészáros & Rees 1997, Vietri 1997, Tavani 1997, Waxman 1997; Wijers, Rees & Mészáros 1997). The optical and X-ray light curves presented by many authors (e.g. Pedersen et al. 1997, Piro et al. 1997, Garcia et al. 1997, Bartolini et al. 1998) have provided evidence for occasional departures from the basic overall power-law decay behavior. Such departures, as well as the possibility of temporal power-law decays that are not exclusively determined by the spectral index, have been shown to follow naturally from fireball models where the radiative regime changes, the energy is not distributed isotropically in the ejecta (Mészáros, Rees & Wijers 1997), or where the energy input depends on the Lorentz factor during the brief injection episode of the central engine, leading to refreshed shocks (Rees & Mészáros 1997). Here we go beyond simple analytical asymptotic models, we derive and solve numerically the differential equations for the dynamics of the afterglow in the general case of an inhomogeneous external medium and refreshed shock mechanism, and calculate numerically the light curves arising in such scenarios.

Our previous numerical work (Panaiteescu & Mészáros 1997a,b) on simulations of light curves and spectra was based on a hydrodynamic code (Wen, Panaiteescu & Laguna 1997) that solves the equations of relativistic hydrodynamics and the shock jump conditions. The energy release mechanisms (synchrotron and inverse Compton) were treated as described in Panaiteescu & Mészáros (1997a). A calculation of the spectra and time history of an afterglow from a spherically symmetric shocked fireball is equivalent to

computing a quadruple integral: over the lab frame time, over the structure of the shocked fluid, over the angle relative to the line of sight toward the fireball center (LSC) of symmetry and over the electron distribution. The hydrodynamic timesteps required to propagate the shell of shocked fluid over times that are more than 5 orders of magnitude larger than the shell crossing time and those necessary for an accurate calculation of the radiative losses lead to exceedingly long numerical runs, which are not best suited for an investigation of the effects of the large number of model parameters involved in the typical external shock scenario of GRBs and afterglows (Mészáros & Rees 1993, 1997). The numerical task is even more time-consuming in the case of anisotropic ejecta, where a new integral over the azimuthal angle is added.

To acquire computational speed, we have developed a numerical code that calculates accurately the evolution of the remnant shell's flow Lorentz factor, by solving the equation that gives the evolution of the kinetic energy of the remnant during the ejecta–external medium interaction, with allowance for an energy injection in the reverse shock (Rees & Mészáros 1997), and radiative and adiabatic losses. Anisotropy of the ejecta or of the energy input is included at the simplest level, assuming cylindrical symmetry around an axis that is not necessarily the same as the LSC. Despite the assumed degree of symmetry in the ejecta, the resulting light curves show a great diversity. Possible inhomogeneity of the external medium is considered in the form of a power-law density. To simplify the energy release treatment, we ignore here the inverse Compton scattering of the self-generated synchrotron photons, which is a fairly good assumption, substantiated by our previous results (Panaitescu & Mészáros 1997b). In what follows we describe the analytic treatment of the remnant's dynamics and energetics, derive analytic light curves and present our numerical results. We discuss the effect of model parameters on the features of the numerical light curves, and compare them with the afterglow of GRB 970508.

## 2. Hydrodynamics of the Remnant and Energy Release

The most important parameter characterizing the temporal evolution of the afterglow is the bulk Lorentz factor  $\Gamma$  of the contact discontinuity (CD) between the ejecta and the swept up external matter. The evolution of  $\Gamma$  is determined by two main factors, the hydrodynamics of the shell (including the energy input, adiabatic losses and the deceleration caused by the external medium) and the radiative losses (synchrotron cooling).

### 2.1. Adiabatic remnant

In the absence of a delayed energy injection and of radiative losses (adiabatic remnant), at any time, the total energy of the fireball is constant:  $d[M(\Gamma - 1) + \Gamma U] = 0$ , where  $M = M_0 + M_{ex}$  is the total remnant mass (the sum of the initial ejecta mass  $M_0$  and the swept-up mass  $M_{ex}$ ) and  $U$  is the co-moving frame internal energy of the remnant. The evolution of  $U$  is given by the adiabatic losses and by the heating of the external matter:  $dU = (dU)_{ad} + (dU)_{ex}$ . The jump conditions (Blandford & McKee 1976) at the forward shock (FS) imply that  $(dU)_{ex} = (\Gamma - 1) dM_{ex}c^2$ , where  $c$  is the speed of light, therefore the energy conservation can be written as:

$$(Mc^2 + U) d\Gamma + \Gamma(dU)_{ad} + (\Gamma^2 - 1) dM_{ex}c^2 = 0 , \quad (1)$$

where  $dM_{ex} = 4\pi r^2 \rho_{ex}(r) dr$  and  $(dU)_{ad} = -(\hat{\gamma} - 1) U d(\ln V')_{ad}$ . The first term in equation (1) is the lab-frame change in the kinetic energy, the second represents the adiabatic losses and the third is the total

lab-frame kinetic energy of the shocked EM, including its internal energy. In the above equations  $r$  is the radial coordinate of the thin remnant,  $\rho_{ex} = \rho_d(r/r_d)^{-\alpha}$ ,  $\rho_d$  is the EM density at the deceleration radius  $r_d$ , defined as the radius where the swept up mass is a fraction  $\Gamma_0^{-1}$  of the initial fireball mass  $M_0$ ,  $\Gamma_0$  being its initial Lorentz factor,  $\alpha < 3$  is the EM power-law index,  $\hat{\gamma}$  is the adiabatic index (maintained close to 4/3 even when  $\Gamma \lesssim 2$  by the relativistic electrons) and  $V'$  is the remnant comoving volume. The differential  $d(\ln V')_{ad}$  refers to that part of the comoving volume that is occupied by the already shocked fluid, i.e. it excludes the change in the comoving volume due to the sweeping up of the infinitesimal  $dM_{ex}$ .

The ejecta compressed between the contact discontinuity and the reverse shock (RS) is much denser than the shocked EM and occupies a volume much smaller than the shell of swept up EM. Therefore we shall assume that the remnant volume is practically given by the volume of the shocked EM. We will assume that the density is uniform behind the FS and equal to that set by the jump conditions at the FS. This implies that the comoving density is determined solely by  $\rho_{ex}(r)$  and  $\Gamma$ :  $\rho'(r) = (\hat{\gamma} + 1)^{-1}(\hat{\gamma}\Gamma + 1)\rho_{ex}(r)$ . Using  $d(\ln V')_{ad} = -d(\ln \rho')$ , the adiabatic losses can be written as:

$$(dU)_{ad} = -(\hat{\gamma} - 1) \left( \frac{\alpha}{r} - \frac{\hat{\gamma}}{\hat{\gamma}\Gamma + 1} \frac{d\Gamma}{dr} \right) U dr. \quad (2)$$

The shocked EM mass is given by

$$dM_{ex} = 3 \frac{M_0}{\Gamma_0} \frac{r^{2-\alpha}}{r_d^{3-\alpha}} dr, \quad (3)$$

which allows one to calculate the comoving volume  $V' = M_{ex}/\rho'$ .

## 2.2. Delayed Energy Input

It is possible that the material injected by the cataclysmic event that generates the relativistic fireball does not have a unique  $\Gamma_0$ , and that some material is ejected with lower initial bulk Lorentz factors, down to some limiting  $\Gamma_m$ . Following Rees & Mészáros (1997), we shall consider that all the ejecta has been released impulsively (on a timescale short compared to the afterglow timescale), all at the same location, and with a power-law distribution of energy per unit Lorentz factor  $\Gamma_f$ :  $dE_f \propto \Gamma_f^{-s} d\Gamma_f$ , for  $\Gamma_m < \Gamma_f < \Gamma_d$ , where  $\Gamma_d < \Gamma_0$  is the Lorentz factor of the contact discontinuity at  $r = r_d$  (for reasons given below, we start our simulations at  $r = r_d$ ). The constant of proportionality is determined by the total injected energy  $E_{inj}$ , which will be one of the free parameters of the model. The fluid moving at lower  $\Gamma_f$  lags behind the CD and catches up with it later, as the fireball is progressively decelerated by the interaction with the EM. From the kinematics of the problem, the Lorentz factor of the ejecta that interacts with the RS at radius  $r$  is given by

$$d\Gamma_f = -\frac{\Gamma_f}{2} \left[ (\Gamma_f/\Gamma)^2 - 1 \right] \frac{dr}{r}. \quad (4)$$

The mass injected in the remnant up to radius  $r$  satisfies the differential equation

$$dM_f = F_s(\Gamma_f, \Gamma) M_{inj} \frac{dr}{r}, \quad (5)$$

where

$$F_s(\Gamma_f, \Gamma) = \frac{s}{2} \frac{(\Gamma_f/\Gamma)^2 - 1}{1 - (\Gamma_m/\Gamma_d)^s} \left( \frac{\Gamma_m}{\Gamma_f} \right)^s. \quad (6)$$

Here  $M_{inj}$  is the total mass that is eventually injected in the remnant, which corresponds to an  $E_{inj}$  given by

$$E_{inj} = \frac{s(s-1)^{-1} [1 - (\Gamma_f/\Gamma_d)^{s-1}] \Gamma_f + (\Gamma_f/\Gamma_d)^s - 1}{1 - (\Gamma_m/\Gamma_d)^s} \left( \frac{\Gamma_m}{\Gamma_f} \right)^s M_{inj} c^2. \quad (7)$$

As the shocked shell propagates from  $r$  to  $r + dr$ , the infinitesimal injected mass  $dM_f$  given by equation (5) collides with the shell, increasing the remnant kinetic energy by  $dE_{k,f}$  and its internal energy by  $(dU)_f$ . These infinitesimal energies can be determined from momentum and energy conservation:

$$dE_{k,f} = \Gamma_f [1 - \Gamma^2 (1 - \beta \beta_f)] dM_f c^2, \quad (8)$$

$$(dU)_f = [\Gamma \Gamma_f (1 - \beta \beta_f) - 1] dM_f c^2, \quad (9)$$

where  $\beta$  represents the velocity in units of  $c$ .

### 2.3. Radiative Losses

As mentioned before, we consider here that the shocked fluid cools through adiabatic expansion and emission of synchrotron radiation from electrons accelerated by the FS. There could be some contribution to the early afterglow light curve from electrons accelerated by the RS, but this is soon overcome by the FS emission that shifts toward lower energies, as the remnant is decelerated. It is also possible that instabilities across the CD lead to a mixing of forward and reverse shocked gases so that their emission properties are similar.

We assume that nearly all electrons are shock-accelerated to a power-law distribution of index  $p > 1$ ,  $dN'_e \propto \gamma_e^{-p} d\gamma_e$ , for  $\gamma_m < \gamma_e < \gamma_M$ , where  $N'_e$  is the co-moving electron number density,  $\gamma_e$  is the electron random Lorentz factor, and we ignore a possible tail of thermal electrons with  $\gamma_e < \gamma_m$ . For  $p > 2$ , the less energetic electrons contain most of the energy. The maximum  $\gamma_M$  is determined by the synchrotron losses during the acceleration timescale, and, for most of the afterglow, is several orders of magnitude larger than  $\gamma_m$ . The minimum  $\gamma_m$  is set by parameterizing the total energy density stored in electrons after acceleration, as a fraction  $\varepsilon_{el}$  of the internal energy density of the shocked fluid, which is given by the jump conditions at shock – Blandford & McKee 1976. The result is:

$$\gamma_m = \frac{p-2}{p-1} \frac{1 - (\gamma_M/\gamma_m)^{1-p}}{1 - (\gamma_M/\gamma_m)^{2-p}} \left[ 1 + \varepsilon_{el} \frac{m_p}{m_e} (\Gamma - 1) \right] \stackrel{p \gtrsim 2}{\sim} \varepsilon_{el} \frac{p-2}{p-1} \frac{m_p}{m_e} (\Gamma - 1), \quad (10)$$

$m_p$  and  $m_e$  being the proton and electron masses, respectively.

The comoving magnetic field  $B$  is assumed to be turbulent and is parameterized through the fraction  $\varepsilon_{mag}$  of the internal energy that is in the form of magnetic field energy,

$$B = \sqrt{8\pi \varepsilon_{mag} \frac{U}{V'}} = B_0 \left[ \varepsilon_{mag} \frac{\hat{\gamma} \Gamma + 1}{\hat{\gamma} - 1} \frac{(3 - \alpha) a^{-\alpha}}{3a^{3-\alpha} - \alpha} u \right]^{1/2}, \quad (11)$$

where  $B_0 = (8\pi \Gamma_0 \rho_d c^2)^{1/2}$ , and the non-dimensional variables  $a = r/r_d$  and  $u = U/M_0 c^2$  have been used.

The radiative losses are given by a double integral over the remnant volume and the electron distribution,

$$(dU)_{rad} = - \int dV' \int_{\gamma_m(t')}^{\gamma_M(t')} dN'_e(\gamma_e) P'_{sy}(\gamma_e) dt', \quad (12)$$

which can be calculated for given  $B$  and  $dN'_e(\gamma_e)$  at each point in the shocked structure. In equation (12),  $P'_{sy}(\gamma_e) \propto \gamma_e^2 B^2$  is the synchrotron power and  $dt' = (\Gamma^2 - 1)^{-1/2} dr/c$  is the comoving frame infinitesimal time.

#### 2.4. Differential Equations and Initial Conditions

We can now add the contribution of the material injection at the RS given by equation (8) to the evolution of  $\Gamma$  (eq. [1]), and obtain:

$$\frac{d\Gamma}{da} = \frac{\Gamma_f [1 - \Gamma^2 (1 - \beta\beta_f) F_s(\Gamma_f, \Gamma)] \omega_M + (\hat{\gamma} - 1) \alpha \Gamma u - 3(\Gamma^2 - 1) \Gamma_0^{-1} a^{3-\alpha}}{a [\mu + (\hat{\gamma}^2 \Gamma + 1)(\hat{\gamma} \Gamma + 1)^{-1} u]}, \quad (13)$$

where  $\mu = M/M_0$  is the dimensionless remnant mass and  $\omega_M = M_{inj}/M_0$  is the dimensionless total injected mass. We can also obtain the differential equation for  $U$  by including the internal energy input (eq. [9]) and the radiative losses (eq. [12]):

$$\frac{du}{da} = [\Gamma_f \Gamma (1 - \beta\beta_f) - 1] F_s(\Gamma_f, \Gamma) \frac{\omega_M}{a} - (\hat{\gamma} - 1) \left( \frac{\alpha}{a} - \frac{\hat{\gamma}}{\hat{\gamma} \Gamma + 1} \frac{d\Gamma}{da} \right) u + 3a^{2-\alpha} \frac{\Gamma - 1}{\Gamma_0} + \left( \frac{du}{da} \right)_{rad}. \quad (14)$$

The first term in the denominator of equation (13) and the first term in the right hand side of equation (14) are switched off when  $\Gamma_f$ , calculated by integrating equation (4), drops below  $\Gamma_m$ . The differential equation for the mass of the remnant can be obtained with the aid of equations (3) and (5):

$$\frac{d\mu}{da} = \frac{3(a^{3-\alpha} - 1)}{(3 - \alpha)\Gamma_0} + F_s(\Gamma_f, \Gamma) \frac{\omega_M}{a}. \quad (15)$$

Solving the hydrodynamics of the remnant is therefore equivalent to integrating the set of coupled differential equations (4), (13), (14) and (15). These equations are valid in any relativistic regime. Before the RS crosses the ejecta ( $r < r_d$ ), the yet unshocked part of the ejecta and the shocked fluid move with different Lorentz factors. To avoid unnecessary complications, we simulate the dynamical evolution of the fireball starting from  $r = r_d$  and pass over the  $r < r_d$  stage by making an appropriate choice of the initial conditions at  $r = r_d$ . These initial conditions are determined by the definition of  $r_d$ . The energy released before  $r_d$ , i.e. before the RS sweeps up the entire fireball, can be safely neglected, so that, by equating the sum of the kinetic energy  $(1 + \Gamma_0^{-1})(\Gamma_d - 1)M_0c^2$  and the lab frame internal energy  $\sim \Gamma_d(\Gamma_d - 1)(M_0/\Gamma_0)c^2$  at  $r_d$  with the initial energy  $E_0 = (\Gamma_0 - 1)M_0c^2$ , it is straightforward to show that  $\Gamma_d = 0.62\Gamma_0$  and  $U(r_d) = (\Gamma_d - 1)(M_0/\Gamma_0)c^2 \sim 0.62M_0c^2$ . Therefore the initial conditions are

$$\Gamma(a = 1) = \Gamma_f(a = 1) = 0.62\Gamma_0, \quad u(a = 1) = 0.62, \quad \text{and} \quad \mu(a = 1) = 1 + \Gamma_0^{-1}. \quad (16)$$

### 3. Analytical Asymptotic Light-Curves

The temporal history of the afterglow flux received at Earth can be calculated analytically by assuming that the ejecta is either spherically symmetric or is a jet with axial symmetry, and that  $\Gamma$  is power-law in  $r$ . The last assumption is correct only over a certain range of times; a different treatment is needed when the remnant slows down to non-relativistic speeds. We consider here relativistically expanding remnants, and for simplicity, in this section we neglect energy injection and restrict our attention to the case when the

remnant is adiabatic, as it is most likely that this stage lasts the longest (Waxman, Kulkarni & Frail 1997). Electrons can be either radiative or adiabatic. The former case is compatible with the assumption of an adiabatic remnant provided that electrons are not re-energized after shock acceleration or that  $\varepsilon_{el}$  has low values, so that most of the internal energy is stored in protons and magnetic fields and lost adiabatically.

For a relativistic and adiabatic remnant, to a good approximation, the Lorentz factor of the CD evolves as (Mészáros et al. 1997)

$$\Gamma \sim \Gamma_d (r/r_d)^{-(3-\alpha)/2}, \quad (17)$$

where  $\alpha < 3$ . The definition of  $r_d$  gives  $r_d \propto (E_0 n_d^{-1} \Gamma_0^{-2})^{1/(3-\alpha)}$ , where  $n_d$  is the EM particle density at  $r_d$ . Using the relationship between the observer time  $T$  and the lab-frame time  $t$ ,  $T \propto t/\Gamma^2$ , the  $T$ -dependence of the Lorentz factor is found to be

$$\Gamma \sim \left[ (E_0/n_d) T^{-(3-\alpha)} \right]^{1/(8-2\alpha)}. \quad (18)$$

Note that  $\Gamma$  is independent on  $\Gamma_d$  (and thus on  $\Gamma_0$  as well). As seen by the observer, the (transverse) source size scales as  $\Gamma T$  if the ejecta is spherically symmetric. The received flux  $F_{\nu_p}$  at the peak  $\nu_p$  of the synchrotron spectrum is  $F_{\nu_p} \propto (\Gamma T)^2 \Gamma^3 I'_{\nu'_p}$  (Mészáros et al. 1997), where  $I'_{\nu'_p}$  is the comoving synchrotron intensity at the comoving peak frequency  $\nu'_p$ .

**Radiative Electrons.** If electrons are radiative,  $I'_{\nu'_p} \propto N'_e (P'_{sy}/\nu'_p) t'_{sy}$ , where  $t'_{sy}$  is the comoving synchrotron cooling timescale. Using equations (10) (with  $p > 2$ ), (11) and (18), and the fact that  $P'_{sy} t'_{sy} \propto \gamma_m$ , one can calculate  $I'_{\nu'_p}$ . The evolution of the observed peak  $\nu_p \propto \gamma_m^2 B \Gamma$  of the synchrotron emission can be obtained in a similar manner. If observations are made at a frequency  $\nu < \nu_p$ , the observer “sees” the low energy tail of the synchrotron spectrum, which has a slope of 1/3. Then  $F_{\nu} = (\nu/\nu_p)^{1/3} F_{\nu_p}$ , leading to

$$F_{rad}(\nu < \nu_p) \propto \varepsilon_{mag}^{-\frac{2}{3}} \varepsilon_{el}^{-\frac{5}{3}} E_0^{\frac{1}{3}} T. \quad (19)$$

Above  $\nu_p$ , the synchrotron spectrum has a slope  $-p/2$ , yielding:

$$F_{rad}(\nu > \nu_p) \propto \varepsilon_{mag}^{\frac{p-2}{4}} \varepsilon_{el}^{p-1} E_0^{\frac{p+2}{4}} T^{-\frac{3p-2}{4}}. \quad (20)$$

Note that  $F_{rad}(\nu)$  is independent on the EM parameters  $\alpha$  and  $n_d$ , and depends strongly (powers close to or above 1) on  $\varepsilon_{el}$  and also on  $E_0$  for  $\nu > \nu_p$ .

**Adiabatic Electrons.** If electrons are adiabatic,  $I'_{\nu'_p} \propto N'_e (P'_{sy}/\nu'_p) \Delta'$ , where  $\Delta'$  is the comoving remnant thickness and  $P'_{sy}/\nu'_p \propto B \propto (\varepsilon_{mag} n_d r^{-\alpha})^{1/2} \Gamma$ . The product  $N'_e \Delta'$  can be calculated using the fact that  $4\pi N'_e m_p r^2 \Delta'$  is the EM mass swept up until radius  $r$  was reached. Below the spectral peak

$$F_{ad}(\nu < \nu_p) \propto \varepsilon_{mag}^{\frac{1}{3}} \varepsilon_{el}^{-\frac{2}{3}} \left[ E_0^{\frac{2}{3}(5-2\alpha)} n_d^2 \right]^{\frac{1}{4-\alpha}} T^{\frac{2-\alpha}{4-\alpha}}. \quad (21)$$

For observations made above  $\nu_p$ , the synchrotron spectrum has a slope  $-(p-1)/2$ , therefore:

$$F_{ad}(\nu > \nu_p) \propto \varepsilon_{mag}^{\frac{p+1}{4}} \varepsilon_{el}^{p-1} \left[ E_0^{p+3-\frac{\alpha}{4}(p+5)} n_d^2 \right]^{\frac{1}{4-\alpha}} T^{-\frac{3}{4}(p-1)-\frac{\alpha}{2(4-\alpha)}}. \quad (22)$$

Generally, the light curve has a strong dependence on  $E_0$  and  $\varepsilon_{el}$ , and also on  $\varepsilon_{mag}$  for  $\nu > \nu_p$ . Other dependences are weak to moderate. For  $2 < \alpha < 3$ ,  $F_{ad}(\nu < \nu_p)$  increases with  $T$ ; the larger  $\alpha$ , the faster  $F_{ad}(\nu > \nu_p)$  decreases with  $T$ .

**Jets.** If the ejecta is jet-like (Rhoads 1997, Waxman et al. 1997), then equations (19) – (22) give the correct observed flux as long as the observer does not see the edge of the jet. For an observer located at an angle  $\theta_{obs}$  relative to the jet axis and a jet of half-angular opening  $\theta_{jet}$  such that  $\theta_{obs} \ll \theta_{jet}$ , the jet edge is seen after  $\Gamma$  drops below  $\theta_{jet}^{-1}$ . In this case, the source size is  $\propto r\theta_{jet} \propto \Gamma^2 T \theta_{jet}$ . The light curve of the afterglow from a jet-like remnant is given by:

$$F_{rad}(\nu < \nu_p) \propto \varepsilon_{mag}^{-\frac{2}{5}} \varepsilon_{el}^{-\frac{2}{3}} \left[ E_0^{\frac{7-\alpha}{3}} n_d^{-1} \right]^{\frac{1}{4-\alpha}} T^{\frac{1}{4-\alpha}}, \quad (23)$$

$$F_{rad}(\nu > \nu_p) \propto \varepsilon_{mag}^{\frac{p-2}{4}} \varepsilon_{el}^{p-1} \left[ E_0^{p+3-\frac{\alpha}{4}(p+2)} n_d^{-1} \right]^{\frac{1}{4-\alpha}} T^{-\frac{3}{2}p - \frac{2-\alpha}{2(4-\alpha)}}, \quad (24)$$

if electrons are radiative and by

$$F_{ad}(\nu < \nu_p) \propto \varepsilon_{mag}^{\frac{7}{8}} \varepsilon_{el}^{-\frac{2}{3}} \left[ E_0^{\frac{22-7\alpha}{6}} n_d \right]^{\frac{1}{4-\alpha}} T^{-\frac{1}{4-\alpha}}, \quad (25)$$

$$F_{ad}(\nu > \nu_p) \propto \varepsilon_{mag}^{\frac{p+1}{4}} \varepsilon_{el}^{p-1} \left[ E_0^{2p+3-\frac{\alpha}{2}(p+2)} n_d \right]^{\frac{1}{4-\alpha}} T^{-\frac{3}{4}(p-1) - \frac{6-\alpha}{2(4-\alpha)}}, \quad (26)$$

if electrons are adiabatic. Note that for a jet, the light curve rises slower and decays faster than for a fireball.

We should keep in mind that equations (19)–(26) were derived assuming that all the electrons are either radiative or adiabatic. The real situation is more complex, as the more energetic tail of the power-law distribution of electrons contains electrons that are radiative and which contribute more to the received flux at some given frequency  $\nu > \nu_p$  than the less energetic electrons, which may be adiabatic. In fact this is the case with most of the numerical X-ray and optical afterglows shown in the next section, at times when the  $\gamma_m$ -electrons are adiabatic and  $\nu_p$  is below the optical band. In a relativistic remnant, the lab-frame synchrotron cooling timescale for electrons radiating at a peak frequency equal to the fixed observing frequency is constant in time, while the adiabatic cooling timescale increases as  $t$ . If the  $\gamma_m$ -electrons are adiabatic, the flux at a frequency where the emission is dominated by more energetic electrons, that are radiative, can be derived using the  $I'_{\nu_p}$  calculated for adiabatic electrons and the fact that the spectrum has a slope  $-(p-1)/2$  for frequencies above  $\nu_p$  and below the peak frequency of the synchrotron emission from electrons that have a radiative timescale equal to the adiabatic one, and a slope  $-p/2$  above this frequency. Interestingly, the result is the same as given by equations (20) and (24) for radiative  $\gamma_m$ -electrons, i.e. only the constant of proportionality is altered. The analytical derivations do not take into account the shape of the equal arrival time surface, i.e. the fact that photons that arrive simultaneously at detector were emitted at different lab-frame times. Moreover, we ignored the fact that there are electrons with Lorentz factors below the  $\gamma_m$  of the freshly accelerated electrons. For these reasons, the equations (19)–(26) are of somewhat limited use and, for more accurate results, one must integrate numerically the afterglow emission.

#### 4. Numerical Results

We have introduced so far the following model parameters: (1) dynamical parameters ( $E_0; n_d; \alpha; \Gamma_0$ ), (2) late energy injection parameters ( $E_{inj}, \Gamma_m, s$ ) and (3) energy release parameters ( $\varepsilon_{mag}; \varepsilon_{el}, p$ ). To these one must add ( $\theta_{jet}, \theta_{obs}$ ) if the ejecta is jet-like. In this section we asses the effect of these parameters, and consider also the situation where  $E_0$  and  $\Gamma_0$  have an anisotropic distribution in the ejecta, which, in the simplest case, introduces one more parameter representing the angular scale of such anisotropy. We

compare our numerical results to the observed X-ray (2–10 keV), optical ( $V$  magnitude) and radio (4.9 GHz) afterglows. We will be looking in particular for the parameter values that yield X-ray and/or optical light curves similar to GRB 970508, for which a fairly uniform time coverage is available.

The simplest case is that of spherically symmetric ejecta with a single impulsive input of energy. Under the simplifying assumptions of a relativistic and adiabatic remnant, the equations (19) – (22) predict the asymptotic radio, optical and X-ray afterglow. For the range of times considered here,  $\nu_p$  is below optical frequencies and only the radio emission shows a peak. This peak generally occurs before  $\nu_p$  reaches few GHz, and it is due to the remnant's transition from the relativistic to the non-relativistic regime. For a homogeneous EM ( $\alpha = 0$ ), radiative electrons and  $p = 2.5$ , the above-mentioned equations for a relativistic remnant yield for  $\nu > \nu_p$  (optical and X-ray fluxes)

$$F_{O,X} \propto \varepsilon_{mag}^{1/8} \varepsilon_{el}^{3/2} E_0^{9/8} T^{-11/8}, \quad (27)$$

while radio flux  $F_R$  is given by equation (19). If electrons are adiabatic, then

$$F_{O,X} \propto \varepsilon_{mag}^{7/8} \varepsilon_{el}^{5/2} E_0^{11/8} n_d^{1/2} T^{-9/8}, \quad (28)$$

$$F_R \propto \varepsilon_{mag}^{1/3} \varepsilon_{el}^{-2/3} E_0^{5/6} n_d^{1/2} T^{1/2}. \quad (29)$$

These analytical approximations are consistent, within their range of validity, with the numerical results shown in Figure 1. For comparison, Figure 1 also shows (with symbols) observational data taken from IAU Circulars, van Paradijs et al. (1997), Sahu et al. (1997), Frail (1997), Piro et al. (1997) or inferred from the data presented by Galama et al. (1997), Bartolini et al. (1998), and Sokolov et al. (1998). As expected from equation (27), fireballs with larger initial energy or energy release parameters yield brighter afterglows. Fireballs with lower electron indices  $p$  lead to afterglows that have a shallower temporal decay (Figure 1[a2]), as predicted by equations (20) and (22). Note that graph (b1) shows that when the electrons emitting at fixed frequency (here, in X-ray) are radiative, the afterglow is indeed independent of the external medium parameters  $n_0$  and  $\alpha$ , as predicted by equation (20). For all the the afterglows shown in Figure 1, the  $\gamma_m$ -electrons become adiabatic for  $T$  between 0.1 and 10 days, while the remnant enters the non-relativistic phase at times between 30 and 300 days, when a slow but steady steepening of the light curves can be seen.

We have ignored the effects of low-frequency synchrotron self-absorption in the radio range, therefore the Figures 1(a3) and 1(b3) give essentially an upper limit to the optically thin radio flux expected in this case. A simple analytical derivation of the absorption frequency is straightforward (Mészáros & Rees, 1997), but it can easily lead to misleading results, since the fireball contains electrons with random Lorentz factors that span more than one order of magnitude, all emitting and absorbing the synchrotron radiation. Taking into account only the newly shocked electrons and ignoring a possible low-energy tail of the electron distribution below  $\gamma_m$ , it can be shown (Panaitescu & Mészáros 1997b) that the self-absorption frequency is  $\nu_{ab} \sim 6.4 (10 \varepsilon_{mag})^{1/5} (10 \varepsilon_{el})^{-1} n_0^{3/5} E_{0,52}^{1/5} T^0$  GHz (at redshift  $z = 1$ ) for a relativistic remnant and adiabatic electrons, where  $E_{0,52} = E_0 / (10^{52} \text{ ergs})$  and  $n_0 = n_d / (1 \text{ cm}^{-3})$ . This result is valid until the remnant becomes non-relativistic or until the shocked material escape sideways, if the remnant is a jet. Therefore the optical thickness is  $\tau = 1.6$  at 4.9 GHz for  $\varepsilon_{el} = \varepsilon_{mag} = 0.1$ ,  $n_0 = 1$  and  $E_{0,52} = 1$ , indicating that the radio fluxes shown in Figures 1(a3) and 1(b3) are overestimated by a factor of  $\tau(1 - e^{-\tau})^{-1} \sim 2$ . A post-shock mild re-acceleration of the cooling electrons can further decrease the radio flux by reducing the number of the low energy electrons in the remnant, without changing significantly the emission at higher energies. Given the above mentioned uncertainties about a correct modeling of a possible low energy electron tail

and its effects on calculating  $\nu_{ab}$  and the synchrotron self-absorption optical depth in the radio range, a comparison between the radio numerical afterglows and the observational data would be inconclusive, and we shall focus on the higher wavelength ranges.

In its simplest form considered in Figure 1, the fireball shock model obviously cannot explain departures from the power-law decay, such as observed in the optical afterglow of GRB 970508 near  $T \sim 2$  days. A brightening of the may arise if there is a delayed energy input, as illustrated Figure 2. The energy injection index  $s$  was set equal to a large value so that the input resembles a second relativistic shell that catches up with the initial fireball. For a delayed energy input  $E_{inj}$  comparable to or larger than the energy of the remnant  $E_0$ , the light curves exhibit a bump at the time of interaction between the two shells. The larger  $E_{inj}$  is, the more prominent is the resulting bump. For lower  $\Gamma_m$ , the collision takes place later, and this might explain a secondary departure from a power-law, apparent in the optical afterglow of GRB 970508 at  $T \gtrsim 50$  days, as shown by the thick long dashes line in Figure 2 (the flattening of the light curve could also be due to a constant contribution of the host galaxy – Pedersen et al. 1997). In Figure 2, the minimum Lorentz factor  $\Gamma_m$  was chosen such that the numerical light curve exhibits the brightening observed in the 970508 optical afterglow after  $T = 1$  day. Taken by itself, a good fit to the 970508 optical afterglow can be obtained with the parameters of the solid line (an absorption  $A_V = 0.25$  mag was used, as found by Reichart 1997), but in this example the predicted X-ray afterglow would be weaker than observed.

For times  $T \gtrsim 0.3$  days in Figures 1 and 2, the synchrotron peak  $\nu_p$  is below the optical band, so that for a given flux level at optical frequency, the X-ray flux is determined only by the slope ( $-p/2$  in the case of radiative electrons) of the spectrum above  $\nu_p$ . This suggests that a brighter X-ray afterglow can be simulated by using a flatter electron index  $p$ , as shown by the  $p = 2.1$  case (dotted line). This also leads to a less steep decay of the optical afterglow, which for  $p < 2$  would be clearly inconsistent with the data. Therefore, a good simultaneous fit of the X-ray and optical afterglow does not appear possible by these means. Alternatively, for a given index  $p$  that is consistent with the observed optical decay, larger X-ray fluxes can be obtained by increasing the available energy (initial and/or injected), but this also leads to brighter optical afterglows. A simple scenario which does provide a simultaneous satisfactory fit after a few days assumes a more substantial absorption in the (rest frame)  $V$  band (short dashed line in Figure 2). The  $A_V = 1.7$  mag used for this fit might be due to dust extinction within the host of this burst, if the latter lies beyond an absorbing galaxy, and along the line of sight toward it.

The parameters of the model indicated with short dashed lines in Figure 2, where we considered a constant electron index throughout the entire afterglow, give an acceptable match of the 970508 X-ray afterglow and the decay of its optical light curve, but at early times the numerical optical afterglow is too bright. The only parameter of the model that can alter the flux obtained in a given band without changing the flux in another band is the electron index  $p$ . Within the model developed so far, the observations would suggest that  $p$  is not constant during the entire afterglow, but changes in such a manner that it leads to lower optical fluxes at early times. The index  $p$  could be constant for a single ejection episode, but the physical conditions resulting from a later ejection might be different. A model with this property is shown in Figure 2 with long dashed lines, where it was assumed that the electron index steepens from  $p = 1.9$  to  $p = 2.3$  when the delayed energy input takes over after  $T \sim 2$  days. This leads to a good match of both the optical rise and the subsequent power-law decay, if an absorption  $A_V = 1.4$  at the source redshift is assumed, as well as providing an acceptable fit to the X-ray light curve. As illustrated here for the case of the GRB 970508 afterglow, a comparison between the features exhibited by the observed X-ray and optical light curves allows one to determine step-by-step the model parameters that yield good matches.

Jet-like outflow obviously reduces the energy requirements of fireballs, which, if extending over  $4\pi$  sr,

would require a total energy above  $10^{52}$  ergs to produce the optical fluxes observed in the afterglow of GRB 970508. In Figure 3(a) we show light-curves arising from jet ejecta whose properties are isotropic within the opening angle  $\theta_{jet}$ . From these numerical results, we can draw several conclusions:

(1) As expected, the light curve decay steepens when the observer sees the edge of the jet. This is shown by the departure of the dotted line (jet, observer located on the jet axis) from the thick solid line (isotropic fireball) around  $T = 6$  days. The smaller  $\theta_{jet}$ , the earlier such a steepening occurs.

(2) Jets seen at angle  $\theta_{obs} < \theta_{jet}$  do not exhibit the rise shown by jets with  $\theta_{obs} > \theta_{jet}$ .

(3) The larger  $\theta_{obs}$ , the more delayed and dimmer the afterglow peak. For energies  $E_0 \lesssim 10^{51}$  ergs, the optical emission from jets located at  $z = 1$  that are seen at an angle  $\theta_{obs} > 2\theta_{jet}$ , is unlikely to be detected. The afterglow that fits best the observations is obtained when energy injection is included. The thin solid line in Figure 3(a) is for a total delayed energy input 4 times larger than the initial energy of the jet, leading to a total available energy of  $1.9 \times 10^{51}$  ergs.

In a more realistic scenario, the explosive event that generates the ejecta may lead to an angle-dependent energy distribution, as considered by Mészáros et al. (1997). Figure 3(b) (which is not meant as a fit to the afterglow of GRB 970508), shows the effect of such an anisotropic distribution for the particular choice where the energy per unit solid angle in the jet is an exponential in the polar angle  $\theta$ :  $(dE_0/d\Omega)(\theta) = (dE_0/d\Omega)_{axis} \exp(-\theta/\theta_E)$ . For  $\theta_E > 0$  the angular energy density decreases toward the jet edge while for  $\theta_E < 0$  it increases. The same angular dependence (with the same angular scale  $\theta_E$ ) was assumed for  $\Gamma_0$ . The initial Lorentz factor has no effect on the light curve if the external medium is homogeneous, as shown in the previous section; the motivation for this choice was simply an isotropic mass distribution in the ejecta. To maximize the effect of the anisotropy in the ejecta, the observer was placed on the jet axis, and a large jet opening was chosen in order to separate this effect from the “edge effect”. In all cases, the energy density at  $\theta = 0^\circ$  was set to  $10^{52}/\pi$  ergs/sr, which leads to the following total jet energies:  $E_{0,52} = 1$  for the isotropic distribution ( $\theta_E = \infty$ ),  $E_{0,52} = 0.2$  for  $\theta_E = \theta_{jet}/3$  and  $E_{0,52} = 8.6$  for  $\theta_E = -\theta_{jet}/3$ . The light curve decays agree qualitatively with the results of Mészáros et al. (1997): if  $dE_0/d\Omega > 0$ , then more energy is emitted from fluid moving at larger angles relative to the LSC, arriving later at detector, and yielding shallower decays than in the isotropic case. Conversely, if  $dE_0/d\Omega < 0$ , then most energy is radiated away by the fluid moving close to the LSC; this radiation arrives earlier at the detector and leads to steeper light curve decays.

The case where the observer is located off the jet axis is considered in Figure 3(c). The parameters  $(dE_0/d\theta)_{axis}$  and  $\theta_E$  were chosen so that the total energy of the jet is the same in all cases. The conclusion that can be drawn from Figure 3(c) is that, for all other parameters fixed, the light curve seen by an off-axis observer is determined mainly by the total energy of the jet and not by how this energy is distributed. The ironing out of the details of the angular energy distribution in an axially symmetric jet is due to the differential relativistic beaming of the radiation emitted by fluid moving at angles between  $\theta_{obs} - \theta_{jet}$  and  $\theta_{obs} + \theta_{jet}$  relative to the LSC.

Jets with the parameters given for Figure 3(a) and 3(c) can explain the rise and decay of the light curve of GRB 970508 after  $T \sim 0.5$  days. The emission detected in early part ( $T \lesssim 0.5$  day) of the optical afterglow may be due to some ejected material lying outside the main jet. In Figures 3(a) and 3(c) we show with dot-dashes lines the emission from such a large angle outflow, containing  $E_0 = 7.0 \times 10^{50}$  ergs, ejected isotropically outside of the central jet of opening angle  $\theta_{jet} = 10^\circ$ , whose axis of symmetry is offset by  $\theta_{obs} = 14^\circ$  relative to the LSC. The sum of the light-curves from such a two-component ejecta (central jet and large angle outflow) matches well the features observed in the afterglow of GRB 970508. The X-ray afterglow can be fitted at the same time with the optical one by making an appropriate choice of the

electron index  $p$  in the jet and in the large angle outflow, and of the absorption in the  $V$ -band.

## 5. Conclusions

Previous models of GRB afterglow light curves from cosmological fireball shocks (e.g. Mészáros , Rees & Wijers, 1997; Rees & Mészáros 1997; Sari, Piran & Narayan 1997) have used analytical descriptions based on scaling laws valid in the asymptotic limits. These require simplifying assumptions and involve various undetermined parameters. The most important analytical results on the afterglow light-curve are given in section §3. They should be used with care when making comparisons with observed power-law decays, as electrons with different random Lorentz factors can be in different radiating regimes. Generally, those electrons radiating in optical and X-ray are radiative, while those radiating at radio frequencies are adiabatic, at least as long as the remnant is relativistic. Moreover, the analytical light curves do not take into account the shape of the equal-arrival time surface, and assume that there is a one-to-one correspondence between the lab-frame time of emission and the detector time.

Numerical calculations provide the environment where the assumptions made in analytical derivations can be tested and relaxed, and where results are expected to be more accurate. In some cases, like that of a fireball in a mildly relativistic regime, or like that of jet ejecta seen at an angle  $\theta_{obs} \neq 0^\circ$ , it is cumbersome to obtain analytical results. At the level of numerical calculations, effects arising from the viewing geometry (the equal arrival time surface is not the same as the equal lab-frame time surface) or from details of the energy release (e.g. an accurate tracking of the evolution of the electron random Lorentz factor  $\gamma_e$ ) can be properly accounted for.

We have solved the differential equations for the afterglow evolution and integrated the remnant emission to calculate light-curves with different model parameters. Energy injection (refreshed shocks), angular anisotropy and jet-like structure of the ejecta allow for a variety of possible behaviors of the numerical light curves, even under the assumption of axial symmetry in the remnant. More than one scenario could explain a fairly large fraction of the optical data of the GRB 970508 afterglow. A spherically symmetric ejecta with energy injection up to a total energy of  $3 \times 10^{52}$  ergs, or a jet of opening  $10^\circ$  seen at an angle of  $14^\circ$ , in which energy is injected up to a total of  $\sim 2 \times 10^{51}$  ergs, both located at redshift  $z = 1$ , seem to fit most the mentioned afterglow. Such energies are quite conservative in a cosmological scenario, and clearly do not require any drastic departures from the simple fireball/firejet scenario. Using a variable index of the electron power-law distribution, we obtained a simultaneous good fit of the X-ray and optical afterglow of GRB 970805, if there is a  $V$ -band absorption of 1.4 magnitudes at the source redshift and/or along the line of sight. Synchrotron self-absorption and post-shock re-energization of the electrons can reduce the radio fluxes obtained numerically and yield a better fit of the radio data, but this comparison is much more uncertain and model-dependent.

The first generation of fireball shock models of afterglows were characterized by great simplicity and have predicted power-law decaying light curves. As one would expect, relaxing some of the assumptions that are usually made in the simplest versions of these models, such as isotropy of the ejecta or or constancy of the parameters that quantify the energy release, leads to an improved agreement between numerical results and observations. All of the models presented here still contain simplifying assumptions (e.g. axial symmetry, power-law delayed energy input), which were taken as a starting point in investigating the features of the numerical light curves. While the present data do not require it, relaxing these assumptions could lead to even more diverse afterglow light curves. The variety of behavior exemplified by the models

we have discussed highlights the potential importance of afterglow data as diagnostics for the dynamics and anisotropy of the ejecta, and emphasizes how much more can be learned when the sample has grown larger.

We are grateful to NASA NAG5-2857, NAG 3801 and the Royal Society for support, and R.A.M.J. Wijers for useful comments.

## REFERENCES

Bartolini, C. et al. 1998, in *Gamma-Ray Bursts, Fourth Huntsville GRB Symposium*, eds. Meegan, Preece, & Koshut (New York:AIP), in press (astro-ph/9710313)

Blandford, R. D. & McKee, C. F. 1976, Phys. Fluids, 19, 1130

Frail, D. et al. , 1997, Nature, 389, 261

Galama, T. et al. 1997, Nature, 387, 479

Garcia, M. R. et al. 1997, ApJL, submitted (astro-ph/9710346)

Mészáros , P & Rees, M. J., 1997, ApJ, 476, 232

Mészáros , P., Rees, M. J., & Wijers, R. 1997, ApJ, in press (astro-ph/9709273)

Panaiteescu, A. & Mészáros , P. 1997a, ApJ, 492, 683 (astro-ph/9703187)

Panaiteescu, A. & Mészáros , P. 1997b, ApJ, submitted (astro-ph/9711339)

van Paradijs, J. et al. 1997, Nature, 386, 686

Pedersen, H. et al. 1997, ApJ, 496, in press (astro-ph/9710332)

Piro, L. et al. 1997, A&A, submitted (astro-ph/9710355)

Rees, M. J. & Mészáros , P. 1997, ApJ, submitted (astro-ph/9712252)

Reichart, D. 1997, ApJ, submitted (astro-ph/9712100)

Rhoads, J. E. 1997, ApJ, 487, L1

Sahu, K. C. et al. 1997, Nature, 387, 476

Sari, R., Piran, T., & Narayan, R. 1997, astro-ph/9712005

Sokolov, V. V. et al. 1997, astro-ph/9709093

Tavani, M. 1997, ApJL, 483, L87

Vietri, M. 1997, ApJL, 488, L105

Waxman, E. 1997, ApJ, 485, L5

Waxman, E., Kulkarni, S. & Frail, D. 1997, ApJ, submitted (astro-ph/9709199)

Wen, L., Panaiteescu, A., & Laguna, P. 1997, ApJ, 486, 919

Wijers, R., Rees, M. J. & Mészáros , P. 1997, MNRAS, 288, L51

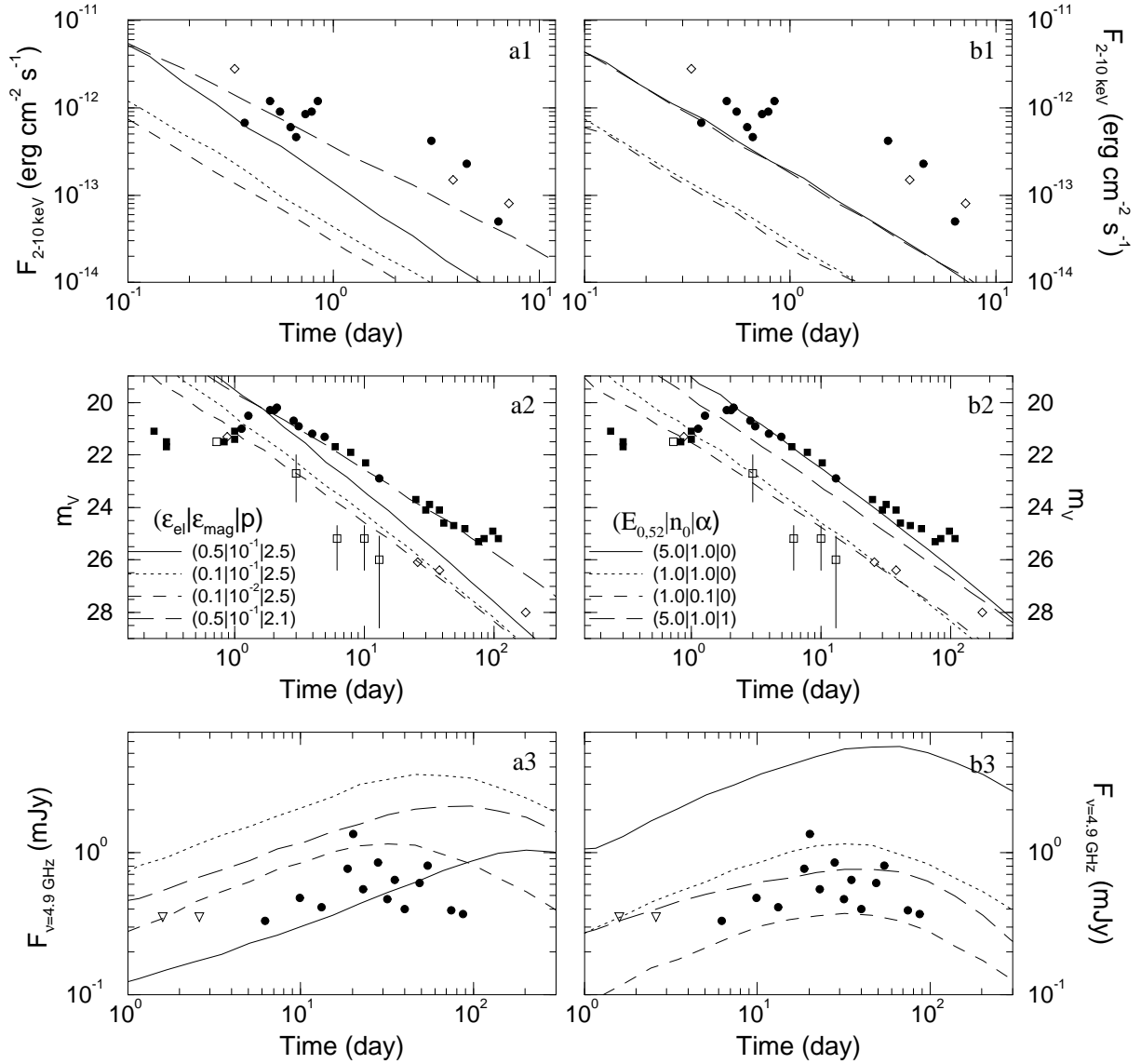


Fig. 1.— The effect of the energy release (left graphs) and dynamical (right graphs) parameters on the afterglow light-curve from a spherically symmetric fireball with no delayed energy input. Legends in the middle graphs give the set of parameters for each curve. For each curve there is another one that differs in only one parameter, allowing assessment of the effect of that particular parameter. Other parameters are:  $E_{0.52} = 1$ ,  $n_0 = 1$ ,  $\alpha = 0$  for graphs (a1)–(a3), and  $\varepsilon_{mag} = 10^{-2}$ ,  $\varepsilon_{el} = 0.1$ ,  $p = 2.5$  for graphs (b1)–(b3). Observational data: open symbols are for GRB 970228, filled symbols for GRB 970508. Graphs (a2) and (b2):  $V$  magnitudes inferred from  $R_C$  magnitudes are shown as squares. Only magnitude errors larger than 0.5 are indicated with error bars. Graphs (a3) and (b3): triangles indicate upper limits. A redshift  $z = 1$  in a  $H_0 = 75 \text{ km s}^{-1} \text{Mpc}^{-1}$ ,  $\Omega = 1$  Universe is assumed. The radio fluxes plotted are the optically thin upper limits; the inclusion of synchrotron self-absorption and/or electron re-energization would lead to lower radio fluxes (§4).

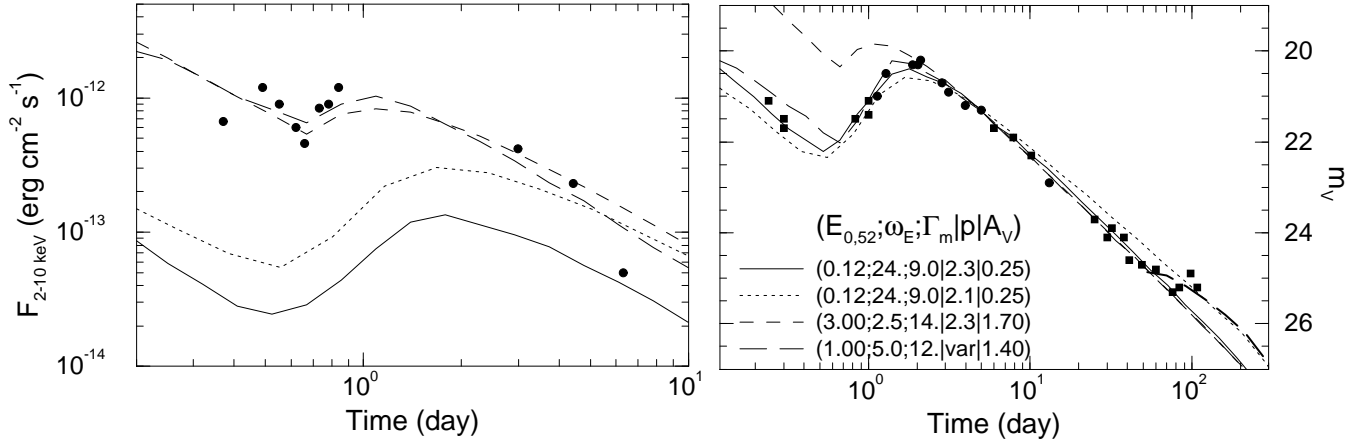


Fig. 2.— Energy injection in an isotropic fireball. The delayed energy input per unit Lorentz factor  $\Gamma_f$  of the ejecta that catches up with the fireball is a power-law in  $\Gamma_f$  (§2.2). The legend gives the initial energy of the ejecta, the total energy injected relative to the initial fireball energy ( $\omega_E = E_{inj}/E_0$ ), the minimum Lorentz factor of the delayed energy input, the index of the power-law distribution of electrons, and the  $V$ -band absorption. The electron index  $p$  is constant in all cases except the one shown with the long dashes line, where it changes from 1.9 to 2.3 at the end of the delayed energy input. Other parameters are:  $\varepsilon_{mag} = 0.1$ ,  $\varepsilon_{el} = 0.1$ ,  $n_0 = 1$ ,  $\alpha = 0$ ,  $z = 1$ . The injection index  $s$  has a large value, leading to an impulsive energy input at  $\Gamma_m$  and to a distinctive brightening of the afterglow. A second impulsive energy input, characterized by  $E_{inj} = 2.5 \times 10^{52}$  ergs and  $\Gamma_m = 3.5$  leads to a temporary flattening of the light curve after  $T \gtrsim 50$  days, as shown by the thick long-dashed line. Symbols represent the data for the GRB 970508 afterglow.

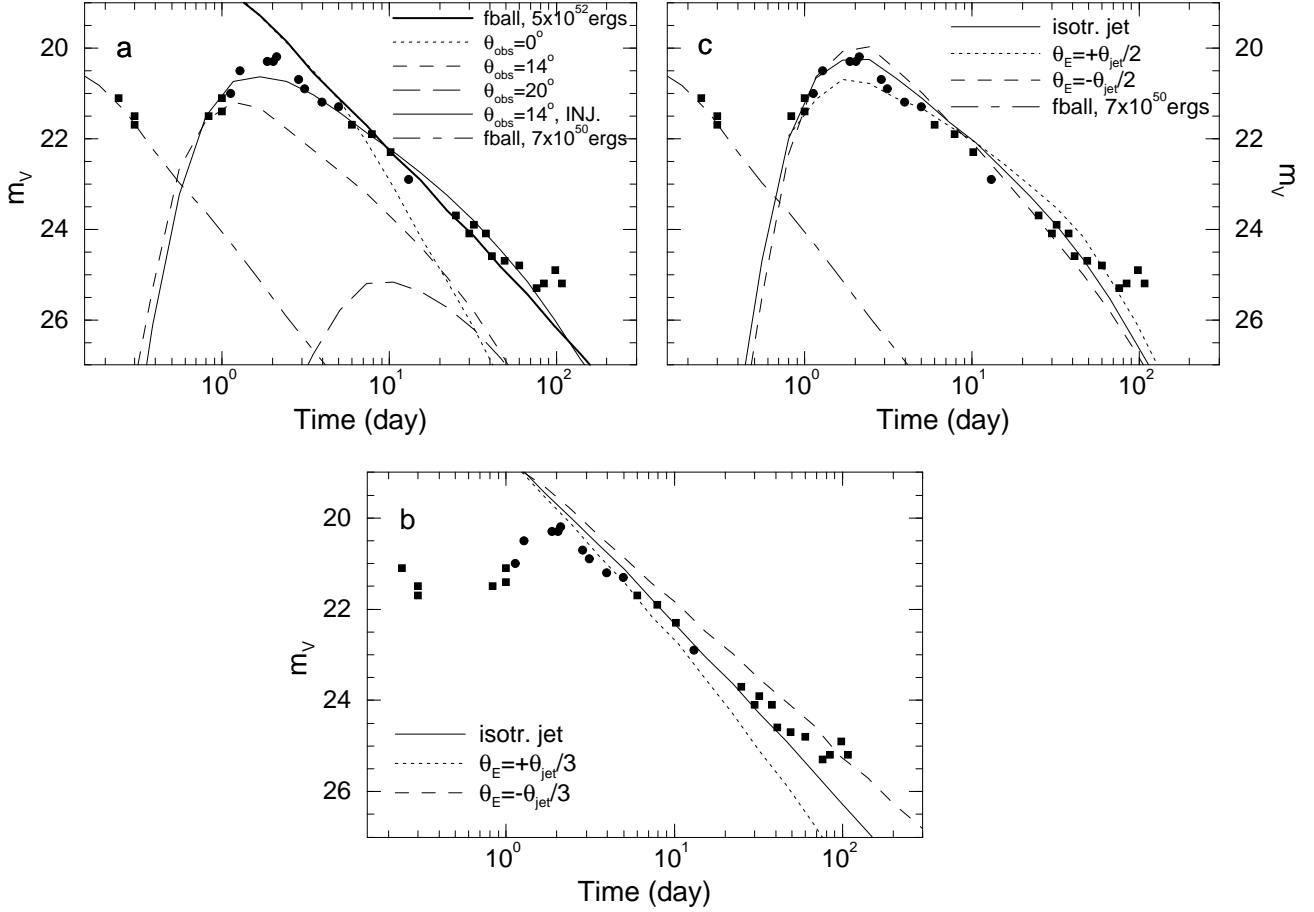


Fig. 3.— Optical light-curves from jet-like ejecta. Comparison data points are for GRB 970508.

(a) An outflow which is isotropic within a jet of half-angular opening  $\theta_{jet} = 10^\circ$ , seen at the different angles, given in the legend. Parameters are  $E_0 = 3.8 \times 10^{50}$  ergs,  $n_0 = 1$ ,  $\alpha = 0$ ,  $\varepsilon_{mag} = 0.1$ ,  $\varepsilon_{el} = 0.1$ ,  $p = 2.5$ ,  $z = 1$ . For comparison, the afterglow from a spherically symmetric remnant with the same parameters, except  $E_0 = 5 \times 10^{52}$  ergs (yielding the same energy density per solid angle), is also shown (solid thick line). The numerical light curve that matches well the observational data (solid thin line) corresponds to  $\theta_{obs} = 14^\circ$  and energy injection characterized by  $E_{inj} = 1.5 \times 10^{51}$  ergs,  $\Gamma_m = 2$  and  $s = 1.5$ .

(b) Effect of an anisotropic angular distribution of energy in a jet with  $\theta_{jet} = 60^\circ$ ,  $\theta_{obs} = 0^\circ$ ,  $(dE_0/d\Omega)_{axis} = 10^{52}/\pi$  ergs/sr. Other parameters ( $n_0, \alpha; \varepsilon_{mag}, \varepsilon_{el}, p$ ) are the same as for graph (a). The legend gives the angular scale  $\theta_E$  (see text).

(c) The same jet as in graph (a), seen at  $\theta_{obs} = 14^\circ$ , but with different energy per solid angle distributions. All jets have the same energy  $E_0 = 1.5 \times 10^{51}$  ergs, isotropically distributed (solid line), exponentially decreasing toward the jet edge (dotted line) or exponentially increasing toward the edge (dashed line).

We have also shown in graphs (a) and (c), with dot-dashed lines, the contribution from an ejecta which is isotropic everywhere outside of the jet with opening angle  $\theta_{jet} = 10^\circ$  and orientation  $\theta_{obs} = 14^\circ$ . The isotropic component has an energy  $7 \times 10^{50}$  ergs (other parameters are as for graph [a]) and can account for the early ( $T \lesssim 1$  day) afterglow emission.